nature catalysis

ARTICLES

https://doi.org/10.1038/s41929-022-00760-z

Check for updates

OPEN

Steering the structure and selectivity of CO_2 electroreduction catalysts by potential pulses

Janis Timoshenko[1,3]✉, Arno Bergmann[1,3], Clara Rettenmaier[1,3], Antonia Herzog[1], Rosa M. Arán-Ais[1], Hyo Sang Jeon[1], Felix T. Haase[1], Uta Hejral[1], Philipp Grosse[1], Stefanie Kühl[1], Earl M. Davis[1], Jing Tian[2], Olaf Magnussen[2] and Beatriz Roldan Cuenya[1]✉

Convoluted selectivity trends and a missing link between reaction product distribution and catalyst properties hinder practical applications of the electrochemical CO_2 reduction reaction (CO_2RR) for multicarbon product generation. Here we employ operando X-ray absorption and X-ray diffraction methods with subsecond time resolution to unveil the surprising complexity of catalysts exposed to dynamic reaction conditions. We show that by using a pulsed reaction protocol consisting of alternating working and oxidizing potential periods that dynamically perturb catalysts derived from Cu_2O nanocubes, one can decouple the effect of the ensemble of coexisting copper species on the product distribution. In particular, an optimized dynamic balance between oxidized and reduced copper surface species achieved within a narrow range of cathodic and anodic pulse durations resulted in a twofold increase in ethanol production compared with static CO_2RR conditions. This work thus prepares the ground for steering catalyst selectivity through dynamically controlled structural and chemical transformations.

Electrochemical energy conversion driven by renewable energy is a cost-effective, environmentally friendly route to convert undesired substances (such as CO_2) into valuable chemicals and fuels. A challenge for the practical application of complex electrochemical processes, such as the CO_2 reduction reaction (CO_2RR) over copper-based catalysts, is control of selectivity[1–5]. One of the critical parameters affecting the catalyst's properties and function—its oxidation state[6,7]—can be conveniently manipulated in situ by choosing appropriate applied potentials. In particular, under pulsed reaction conditions the desired structural motifs and preferred oxidation state can be (re)generated[8–11].

Previous investigations have provided conflicting explanations for the enhancement of catalytic properties under pulsed CO_2RR conditions. Studies employing polycrystalline copper electrodes[8,9,12–18], single crystals[10] and preoxidized copper nanocubes[11,19] revealed enhanced C_{2+} product formation, suppression of the competing hydrogen evolution reaction (HER) and increased stability of catalytic activity under pulsed CO_2RR. These findings were attributed either to the formation of oxidized copper species[10,11,18], to catalyst surface morphology changes[10,19,20], to the removal of poisoning hydrogen and carbon species from the catalyst's surface[8,17], to an enhanced adsorption of OH species and stabilization of CO_2RR intermediates[16], or to the local modulation of the electrolyte pH and CO_2 concentration[17,19,21,22]. The dominant mechanism depends on the parameters of the applied potential (for example, its value, pulse shape and duration of the working and anodic pulses).

In this article we focus on the regime in which the selected anodic potential ($E_a = +0.6$ V versus the reversible hydrogen electrode (RHE)) and the duration of the restoring pulse ($\Delta t_a > 0.5$ s) are sufficient for the generation of copper oxides. Thus, changes in the catalyst surface structure and composition could play a decisive role in the reaction pathway and selectivity. By controlling the type and amount of copper oxide formed during the restoring pulses we steer the CO_2RR selectivity of a Cu_2O nanocube (NC)-derived catalyst. In particular, ethanol formation is doubled (compared with that under stationary conditions) within a narrow range of pulse durations, where a balance between metallic copper and distorted copper oxide species on the catalyst surface is achieved, as revealed by time-resolved operando X-ray absorption spectroscopy (XAS) and high-energy X-ray diffraction (XRD), and supported by quasi in situ X-ray photoelectron spectroscopy (XPS). Our study demonstrates the great potential of pulsed electrolysis for tailoring the catalyst performance and highlights the role of operando investigations for the mechanistic understanding of next-generation catalysts operating under dynamically changing reaction conditions.

Results

Selectivity under static and pulsed reaction conditions. The size-selected (~30 nm) and shape-selected Cu_2O NCs employed in this study (Fig. 1a) were shown to be catalytically active and selective for CO_2RR to C_{2+} products under potentiostatic conditions[19,23,24], but are also well-suited for synchrotron-based operando investigations. Details of the sample preparation and characterization are given in Supplementary Note 1 and Supplementary Fig. 1.

Under static CO_2RR in CO_2-saturated 0.1 M $KHCO_3$ at −1.0 V, a transformation of the crystalline Cu_2O phase to metallic copper was observed by XRD, while XAS showed nearly complete copper reduction at −1.0 V (Supplementary Figs. 2–7)[23,24]. This process is relatively slow: even after 60 min under CO_2RR, peaks of the Cu_2O phase were still present in the XRD pattern (Supplementary Fig. 4), and several hours were required until no further changes were visible in the XAS data (Supplementary Fig. 3 and Supplementary Note 2). The reduction under static CO_2RR also resulted in changes in the catalyst morphology, namely, a partial loss of the cubic shape (Fig. 1b and Supplementary Fig. 1). The selectivity of the reduced catalyst under static conditions was in line with previous reports[24–26].

[1]Department of Interface Science, Fritz-Haber Institute of the Max-Planck Society, Berlin, Germany. [2]Institute of Experimental and Applied Physics, Kiel University, Kiel, Germany. [3]These authors contributed equally: Janis Timoshenko, Arno Bergmann, Clara Rettenmaier. ✉e-mail: janis@fhi-berlin.mpg.de; roldan@fhi-berlin.mpg.de

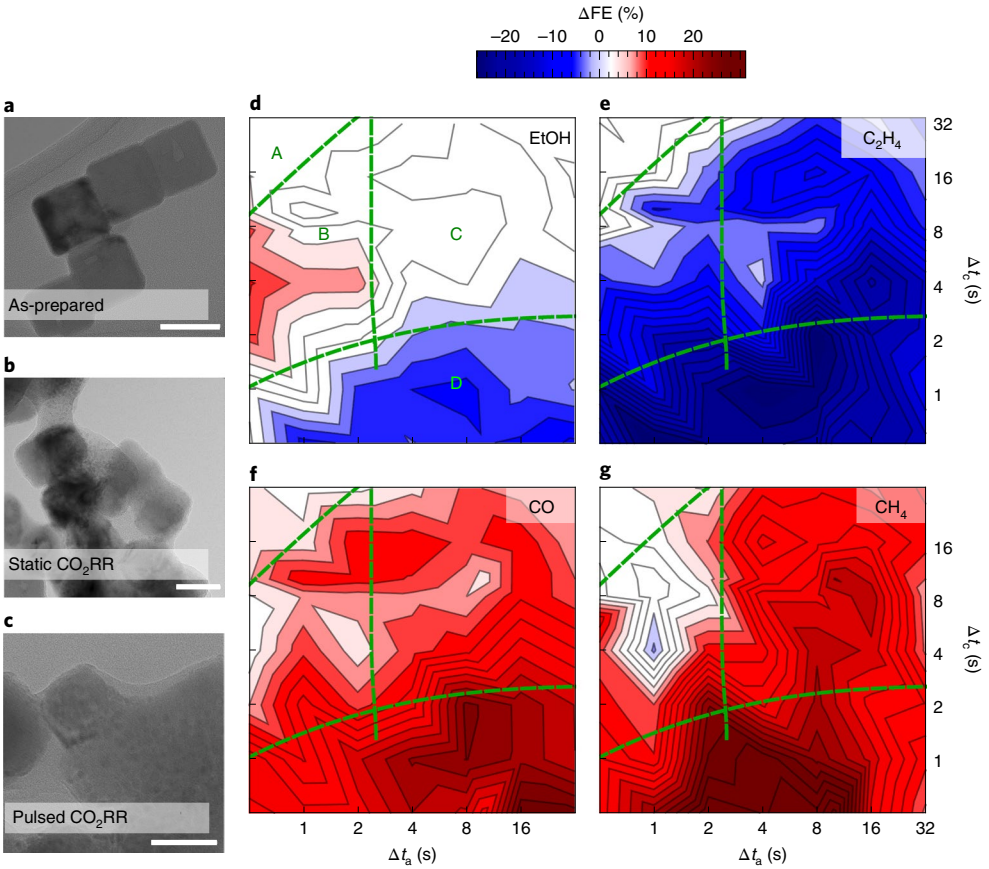

Fig. 1 | Evolution of the catalyst morphology and selectivity under static and pulsed CO_2RR. a–c, Ex situ TEM images of as-prepared Cu_2O NCs (**a**), NCs after CO_2RR for 60 min under static −1.0 V (RHE) potential (**b**) and NCs after pulsed CO_2RR for 60 min ($\Delta t_c = \Delta t_a = 10$ s, $E_c = -1.0$ V and $E_a = +0.6$ V) (**c**). Scale bars correspond to 20 nm. **d–g**, Changes in the FE under pulsed CO_2RR with respect to that under a static −1.0 V potential: excess FE for EtOH (**d**), C_2H_4 (**e**), CO (**f**) and CH_4 (**g**) under pulsed CO_2RR with different lengths of anodic and cathodic pulses (Δt_a and Δt_c, respectively). Regions A–D correspond to distinct regimes with different catalyst surface composition, as explained in the text.

Ethylene (C_2H_4), methane (CH_4) and ethanol (EtOH) were detected as the main CO_2RR products, with Faradaic efficiencies (FEs) of 40%, 20% and 10%, respectively. The FE of H_2 from the competing HER was only 17% (Supplementary Note 3 and Supplementary Table 1).

To the pre-reduced catalyst, we applied a series of oxidizing (anodic) pulses and working (cathodic) pulses with durations Δt_a and Δt_c, respectively. Figure 1d–g shows the difference in the FEs of the products measured under pulsed CO_2RR with varied Δt_a and Δt_c, with respect to the FEs obtained under a static cathodic potential (−1.0 V). The potential values for cathodic and anodic pulses in all cases were $E_c = -1.0$ V and $E_a = +0.6$ V, respectively. The latter is a potential that is expected to oxidize Cu(0) to Cu(I) (Supplementary Note 4 and Supplementary Fig. 8)[10]. The striking feature in Fig. 1 is the distinct dependency of the ethanol FE on the pulse duration. At $\Delta t_a > 2$ s and $\Delta t_c < 2$ s, the formation of ethanol is suppressed. Furthermore, an enhancement in the ethanol FE is observed for $\Delta t_a < 2$ s and Δt_c values between approximately 1 s and 10 s, with a maximum at $\Delta t_a = 0.5$ s and $\Delta t_c = 4$ s, where the ethanol FE is 1.7 times higher than that under static CO_2RR (Fig. 1d). At the same time, the C_2H_4 formation (Fig. 1e) is suppressed under pulsed CO_2RR at all Δt_a and Δt_c. The latter is accompanied by a boost in the C_1 product formation (CO, Fig. 1f and CH_4, Fig. 1g), and the suppression of the H_2 (Supplementary Fig. 9a).

Supplementary Note 3, Supplementary Tables 2 and 3 and Supplementary Figs. 9–15 provide additional details on pulse-length dependencies of the catalyst selectivity. In particular, Supplementary Fig. 9a shows a remarkable independency of the H_2 selectivity on the pulse duration. This indicates that the enhanced ethanol formation observed for $\Delta t_a < 2$ s and $1\text{ s} < \Delta t_c < 10$ s cannot be attributed to changes in the hydrogen coverage or local pH. These effects are considered in the prior literature[8,17,19,21] to explain the changes in CO_2RR under pulsed conditions, but should also affect the HER. While we recognize their importance for pulsed CO_2RR in general, they do not play a decisive role in the ethanol selectivity for the pulse lengths and oxidative potential values used here. We also note here that an oxidation of reaction products and intermediates by anodic pulses cannot be ruled out, but is expected to have only a minor impact (Supplementary Note 1). The FE changes observed in our system thus must stem from two different effects: periodic dynamic changes induced in the catalyst by potential pulses, and the irreversible evolution of the catalyst morphology. Indeed, the ex situ transmission electron microscopy (TEM) images in Fig. 1c and Supplementary Fig. 1 show that exposure of the catalyst to pulsed CO_2RR conditions for 1 h results in a partial loss of the cubic morphology and the formation of a peculiar granular structure, not observed under static CO_2RR. We attribute these to the dispersion/dissolution–redeposition processes that we recently revealed for cubic copper nanostructures under potentiodynamic CO_2RR-related conditions using electrochemical electron microscopy[27–29].

To distinguish the relative contribution to the selectivity of dynamic transformations from the concomitant irreversible structural changes also induced by the pulses, the pulse sequence was interrupted after 1 h and the catalyst selectivity was subsequently

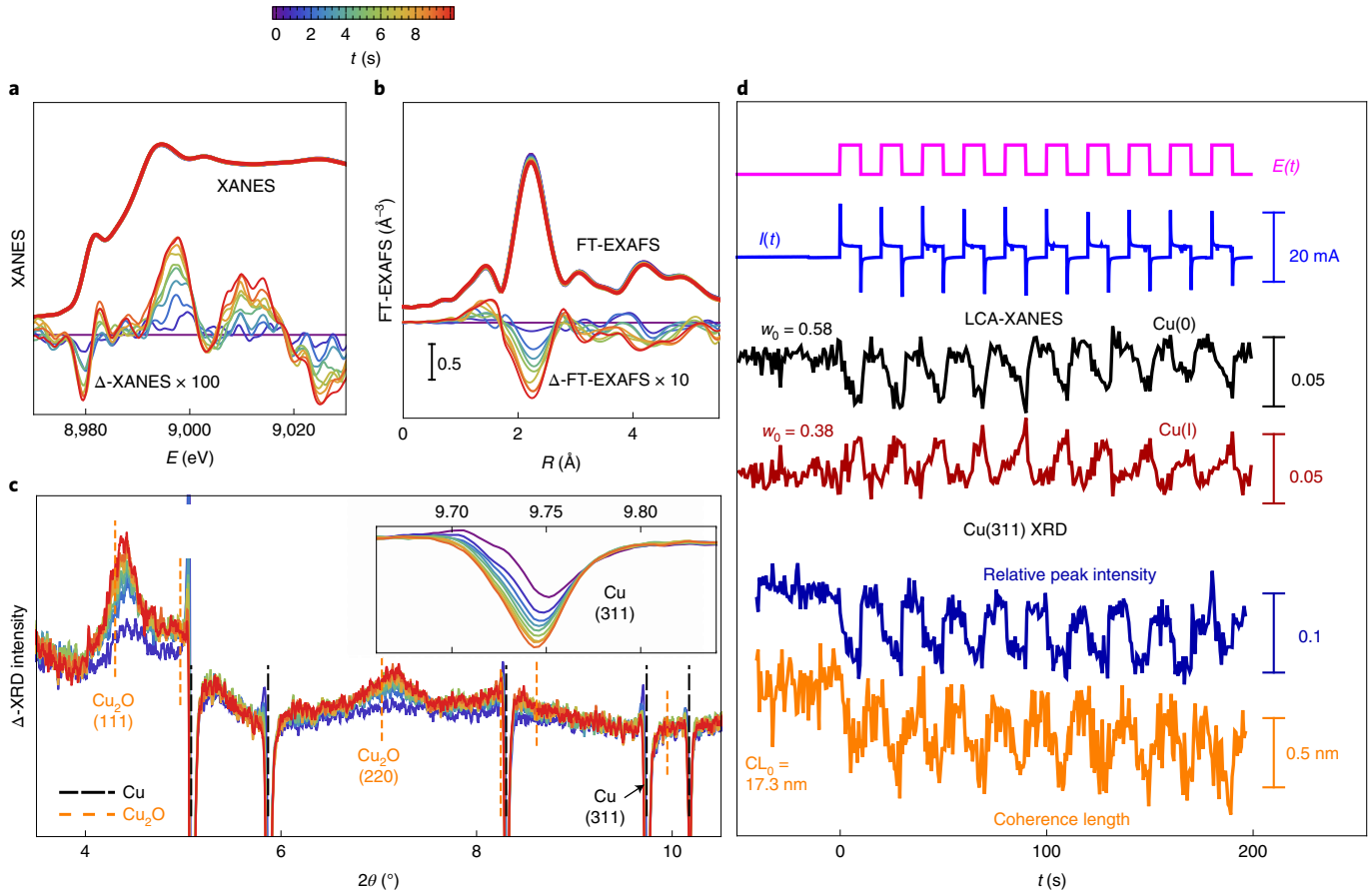

Fig. 2 | Evolution of the operando Cu K-edge XAS and XRD data under pulsed CO_2RR. a–c, Changes in XANES (**a**), EXAFS (**b**) and XRD (**c**) data under an anodic pulse. Data corresponding to different times since the onset of the anodic pulse are shown (see colour bar). Panels **a** and **b** show raw spectra and the differential data, where the XANES or the magnitude of the Fourier-transformed (FT)-EXAFS corresponding to the onset of the anodic pulse ($t = 0$) were subtracted. Panel **c** shows differential XRD patterns, where the XRD intensities corresponding to $t = 0$ were also subtracted. Inset: zoomed-in region corresponding to the (311) Bragg peak for metallic copper. **d**, Time dependencies of the concentrations of Cu(0) and Cu(I) species from XANES analysis, and changes in the area of the Cu(311) Bragg peak as a measure of the amount of metallic copper, and in the coherence length of the metallic copper domains estimated using the Scherrer equation from the width of the Cu(311) Bragg peak. Time dependencies of the applied potential $E(t)$ and measured current $I(t)$ are also shown. w_0 and CL_0 are the concentration and coherence length, respectively, of metallic copper species at $t = 0$. Pulse parameters: $\Delta t_c = \Delta t_a = 10$ s, $E_c = -1.0$ V, $E_a = +0.6$ V.

measured under static CO_2RR conditions after another hour. As shown in Supplementary Figs. 9 and 10, under these conditions the high FE for CH_4 is preserved, while the FE for C_2H_4 remains low. Thus, the enhancement in CH_4 formation and suppression of C_2H_4 must stem from the irreversibly increased surface roughness and granular morphology. Nonetheless, such morphological changes cannot explain the increase in the CO FE, the suppression of HER and the pulse-length-dependent ethanol FE. In fact, when the pulses are interrupted, the FEs of CO and H_2 mostly return to the level observed for a fresh sample under static CO_2RR conditions. Moreover, the ethanol FE under pulsed CO_2RR appears to be a result of two competing mechanisms: irreversible morphological transformations and dynamic processes. The former have a detrimental effect, similarly to the case of C_2H_4 (Supplementary Fig. 9e,f). The latter, within a narrow range of Δt_a and Δt_c values, results in enhanced ethanol formation, and are probably associated with changes in the copper chemical state. Their transient nature requires us to apply operando methods for their investigation.

Catalyst evolution under pulsed reaction conditions. Periodic reversible changes in the catalyst structure and composition under pulsed CO_2RR with $\Delta t_a = \Delta t_c = 10$ s and $E_a = 0.6$ V are evidenced by both XAS (Fig. 2a,b) and XRD (Fig. 2c). In particular, linear combination analysis (LCA) of X-ray absorption near-edge spectroscopy (XANES) data (Fig. 2d) shows that the Cu(I) fraction increases upon applying the anodic pulse, and decreases during the cathodic pulse. An opposite trend is observed in the Cu(0) concentration, while the Cu(II) concentration varies much less (Supplementary Fig. 16). The variations in the fraction of the metallic copper phase and the size of the crystalline copper domains are captured also by the changes in the metallic Cu(311) Bragg peak area and width, respectively. In particular, the amount of metallic copper and the size of the copper domains are smaller under pulsed CO_2RR with respect to those during the static CO_2RR at −1.0 V. Similar variations in the catalyst composition and structure were observed for longer ($\Delta t_a = \Delta t_c = 30$ s) and shorter ($\Delta t_a = \Delta t_c = 1$ s) pulses (Supplementary Figs. 16–18).

Furthermore, for all pulse durations with $\Delta t_a = \Delta t_c$, the periodic variations of the Cu(I) and Cu(0) concentrations were not accompanied by accumulation of oxide: all oxide species generated during the anodic potential pulse were removed during the subsequent cathodic pulse. The removal of the electrochemically grown oxide species is quick, which contrasts with the sluggish initial reduction of the Cu_2O phase under the static CO_2RR. This implies that only

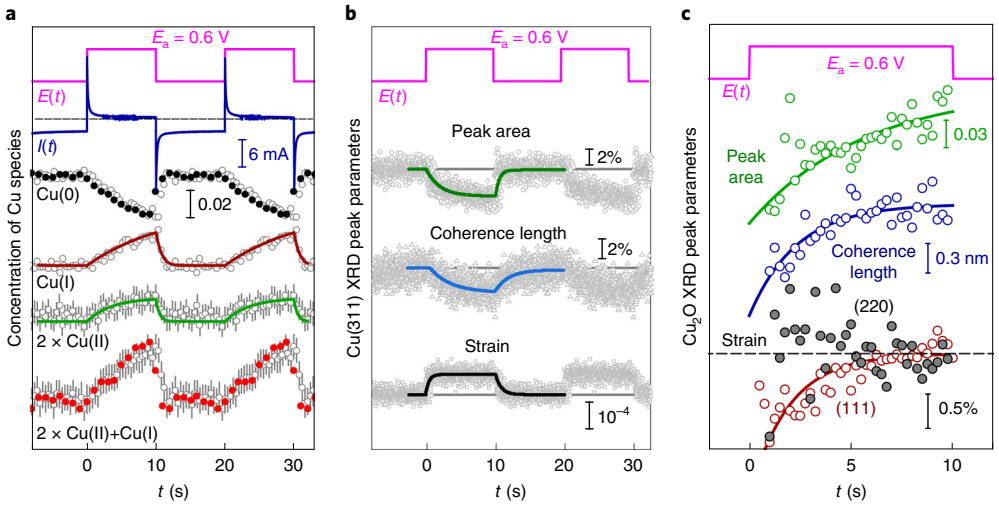

Fig. 3 | Variations in catalyst structure and composition during potential pulse. a, LCA-XANES analysis results (grey open circles) for averaged data for NCs under CO_2RR with pulse lengths $\Delta t_a = \Delta t_c = 10$ s, $E_c = -1.0$ V and $E_a = 0.6$ V. Results of EXAFS data fitting (filled black and red circles show the Cu(0) and total Cu(I) and Cu(II) concentrations extracted from Cu–Cu and Cu–O coordination numbers, respectively). Solid lines display the result of fitting concentration profiles for Cu(I) (red line) and Cu(II) (green line) with an analytical model. The concentration profile for Cu(II) is multiplied by 2 for clarity and to account for the twofold larger Cu–O coordination number in CuO than in the Cu_2O bulk structure. Depicted error bars reflect the standard errors of LCA-XANES fitting results. The time dependencies of the potential $E(t)$ and the current $I(t)$ are also shown (vertical bars show the scale for different datasets). **b**, Evolution of the Cu(311) Bragg peak parameters. The relative changes in the Bragg peak area, the copper coherence length and the lattice strain are depicted. **c**, Evolution of the Cu_2O-like Bragg peak parameters during the anodic pulse. The total area of the (111) and (220) Bragg peaks, average coherence length extracted from the (111) and (220) peak broadenings, and the lattice strain for the (111) and (220) lattice spacings are shown. The solid lines in **b** and **c** are guides for the eye (exponential fits).

the near-surface layers of the catalyst (up to 0.5 nm, as estimated from the changes in coherence length) are reoxidized during the anodic pulse, while the metallic core structure is maintained. The structure and properties of this electrochemically formed surface oxide probably differ noticeably from the properties of the bulk-like Cu_2O phase in the as-prepared NCs, making it easier to reduce. The formation of a thicker oxide layer can be achieved by increasing the anodic potential value (Supplementary Fig. 19e and Supplementary Note 5)[19]. The catalyst properties in this regime of higher E_a values might differ strongly from those of the system exposed to $E_a = 0.6$ V pulses, and are beyond the scope of this paper.

Characteristic time scales of catalyst transformations. To better understand the periodic changes in the catalyst structure, we averaged the XAS and XRD data points collected at the same times after the onset of each pulse cycle (Fig. 3 and Supplementary Figs. 20–24). The LCA-XANES method and extended X-ray absorption fine structure (EXAFS) data fitting for the averaged data (Supplementary Fig. 20) both revealed the oxidation of copper species and Cu–O bond formation during the anodic pulse, and are in excellent quantitative agreement (Fig. 3a and Supplementary Fig. 22). The periodic reoxidation of the catalyst is also observed in XRD, as evidenced by the changes in the metallic copper phase (Fig. 3b and Supplementary Fig. 23), but also by the appearance of Bragg peaks from a Cu_2O-like phase (Fig. 3c).

Although the spike in the current $I(t)$ detected upon changing the applied potential and mostly related to double-layer charging is relatively short (<1 s, Fig. 3a), the transformations of the catalyst structure and composition are much slower. Moreover, a strong asymmetry between the oxidation and reduction processes was observed, with the latter being significantly faster. Indeed, although 10–20 s of the anodic potential with $E_a = 0.6$ V are required for the oxidation to reach its stationary value, the complete removal of the oxide species generated is achieved within 1–2 s of the cathodic pulse. Similarly, the intensity of the XRD peaks corresponding to the metallic copper lattice decreases within 10–20 s upon application of the anodic pulse, and increases back rapidly, within 1–2 s, upon the onset of the cathodic pulse (Fig. 3b and Supplementary Fig. 23). When comparing the results for different pulse lengths, we observe that the characteristic reduction and oxidation times are independent of the pulse length (Supplementary Fig. 24), and thus can be used as descriptors of a particular sample under a given oxidizing potential (E_a). The XAS and XRD results are also confirmed by quasi in situ XPS measurements (Supplementary Fig. 25 and Supplementary Note 6). In particular, at all pulse lengths, the surface-sensitive XPS method shows much higher variations in the cationic copper concentration due to the potential pulse than the bulk-sensitive XAS, providing important evidence that catalyst oxidation is limited to its surface.

Moreover, even at $E_a = 0.6$ V, not only Cu(I) species but also some Cu(II) is created during the anodic pulse, as evident from XANES, but also confirmed by observed variations in the Cu–O bond length in the EXAFS data (Supplementary Fig. 26). The presence of these Cu(II) species is attributed to the unique surface morphology adopted by the NCs under the harsh pulsed reaction conditions. Cu(II) species are likely to be unstable, as noted in cyclic voltammetry experiments where different Cu oxidation states were tracked by XAS (Supplementary Note 4) and the generation of Cu(II) coincided with the loss of copper fluorescence intensity. Indeed, inductively coupled plasma mass spectrometry (ICP-MS) analysis of the copper concentration in electrolyte after CO_2RR shows partial catalyst dissolution under all pulsed regimes investigated (Supplementary Note 7 and Supplementary Table 4), signalling the appearance of unstable species during the anodic pulse. Due to their continuous regeneration, the importance of these species for catalytic activity cannot be excluded. We observe no delay between the formation of Cu(I) and Cu(II) species. In fact, it appears that the generation of Cu(II) species starts slightly before that of Cu(I) species. This suggests that instead of the gradual oxidation [Cu(0) → Cu(I) → Cu(II)], the generation of Cu(II) species is a separate, independent process

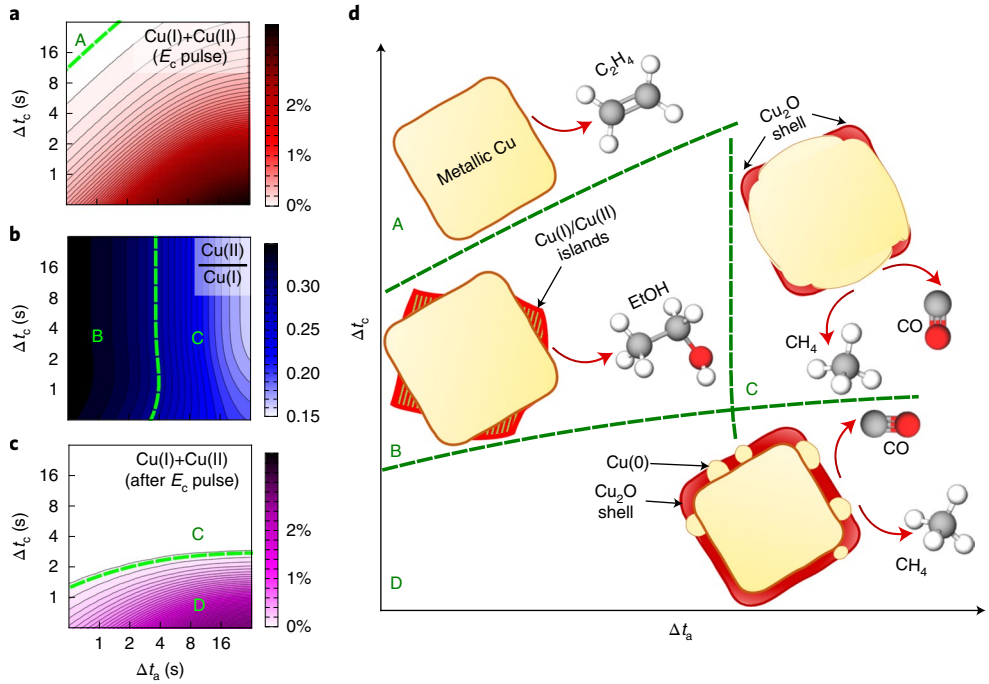

Fig. 4 | Effect of the durations of the anodic (Δt_a) and cathodic (Δt_c) pulses. a–c, Results obtained from the analysis of XAS data for copper NCs during pulses with $E_a = 0.6$ V, showing the average concentration of the oxide species present during the cathodic pulse (**a**), the ratio of Cu(II) and Cu(I) concentrations during the cathodic pulse (**b**) and the concentration of oxide species that remains after the *n*th cathodic pulse is completed (**c**). **d**, Schematic depiction of the catalyst structure and composition during a cathodic pulse extracted from XAS and XRD data. The ranges of Δt_a and Δt_c values corresponding to each regime are indicated in **a**–**c**.

[Cu(0) → Cu(II)]. The independence of the Cu(0) → Cu(II) and Cu(0) → Cu(I) processes is also observed in the cyclic voltammetry experiments (Supplementary Note 4). This leads to a situation that during the short anodic pulse, the concentrations of the Cu(I) and Cu(II) species are comparable, although at large Δt_a values the concentration of Cu(I) is much higher than that of Cu(II). Indeed, in the dataset corresponding to 1 s pulses (Supplementary Fig. 22a) the variations in Cu(II) species concentrations seem to be as pronounced as those in the Cu(I) concentration. With increasing E_a, the contribution of Cu(II) species increases strongly (Supplementary Fig. 22d). The generation of Cu(II) species at $E_a = 1.0$ V is clearly faster than that of Cu(I) species at $E_a = 0.6$ V, resulting in a steeper drop in the Cu(0) concentration when an anodic pulse is applied (Supplementary Note 5).

We conclude that under CO_2RR pulses with $E_a = 0.6$ V, a layer of oxide with mixed valence state (Cu(I)/Cu(II)) is formed on the surface of the copper NCs. Further insights into the structure of this oxide can be extracted from the XRD measurements. The area of the Bragg peaks attributed to Cu_2O shows similar kinetics (with opposite sign) to that of metallic copper (Fig. 3b,c). The coherence length of the CuO_x phase increases within the entire 10 s anodic pulse, reaching ~3 nm at the end of the pulse. At the same time we observe a gradual expansion of the oxide lattice, as determined from the position of the Cu_2O(111)-like Bragg peak. Importantly, the Cu_2O(220)-like Bragg peak position follows a different trend: the (220) lattice expands during the first 2–3 s upon the application of the anodic pulse, and then slightly shrinks. This suggests a distortion of the Cu_2O-like phase in the early stages of the anodic pulse, which we associate with the growth of (111)-oriented Cu_2O on the metallic Cu(100) surfaces[30,31]. The lattice mismatch between Cu(100) and Cu_2O(111) induces the in-plane expansion and a relatively larger Cu_2O-like (220) lattice spacing. The reduced (111) lattice spacing in the early stages of the anodic pulse might, in turn, be a consequence of a tilted growth axis which differs slightly from the surface normal and leads to anisotropic compressive strain in the oxide lattice[30–32]. As the oxide layer grows thicker, the distortion gradually diminishes, leading to a rather bulk-like Cu_2O after 10–20 s. Changes in the lattice spacing in metallic copper under pulsed CO_2RR are also observed, but are quite different from those in the oxide phase. In particular, the copper lattice expansion upon the application of the anodic pulse is faster than the changes in the Cu_2O(111) Bragg peak position (Fig. 3b,c), and the expansion magnitude practically does not depend on the anodic pulse length (Supplementary Fig. 24). This expansion appears to be independent from the copper oxidation process and reflects the charging of the Cu/CuO_x interface.

Linking the catalyst's structural evolution to its selectivity. Considering that the oxidation and reduction rates do not depend on the pulse length, we estimate them from the XAS data collected during pulsed CO_2RR with the largest Δt_a and Δt_c values (30 s), and propose a simple kinetic model to predict the time dependencies of the concentrations of Cu(0), Cu(I) and Cu(II) species at arbitrary Δt_a and Δt_c (Supplementary Note 8, Supplementary Fig. 27 and Supplementary Table 5). Knowing the latter, we can now focus on: (1) the average concentration of copper oxide species present during the cathodic pulse, (2) the ratio of the Cu(II) and Cu(I) content during the cathodic pulse and (3) the concentration of oxide species remaining after the cathodic pulse is completed (Fig. 4a–c). Based on these results and the catalytic selectivity data in Fig. 1d–g, we identify four regimes (A–D, Fig. 4a–c) with distinct catalytic properties, which stem from distinct catalyst surface compositions. The latter are schematically depicted in Fig. 4d. In particular, the enhanced ethanol production at low Δt_a and intermediate Δt_c values (region B) is attributed to an optimal balance between oxidized and reduced copper species on the catalyst surface, and the presence of a distorted copper oxide phase.

At larger Δt_c (region A), in the absence of the effect of an irreversible morphology change, the FEs for all CO_2RR products become similar to those observed under static CO_2RR. Here the catalyst is on average completely metallic, and dynamic changes associated with the pulsed protocol take place for proportionally shorter times and cannot affect the catalyst performance noticeably. However, at shorter Δt_c, the oxide species created on the catalyst surface during the anodic pulse have a pronounced impact. Note that the formation of a complete monolayer of surface oxide on cubic nanoparticles ~30 nm in size is equivalent to an increase in the oxide concentration by ~3%, which is in good agreement with the maximal increase in the oxide fraction observed in Fig. 4a for pulses with $\Delta t_a \gg \Delta t_c$, suggesting that the catalyst surface is completely oxidized during the anodic pulse in this case. During the subsequent cathodic pulse, the surface is completely (region C) or partially (region D) re-reduced, recovering the metallic copper sites active for CO_2RR. The presence of metallic islands on the catalyst surface in direct contact to copper-oxide-rich surface regions during the working pulse has a beneficial effect for CO formation. In particular, the pulse-duration dependency of the excess FE for CO (Fig. 1f) has a similar profile as the pulse-duration dependency of the oxide fraction present during the working pulse (Fig. 4a), where an increase in the oxide fraction results in an enhanced CO formation. The latter observation is in agreement with the results obtained under pulsed CO_2RR for a copper foil, where the CO production was favoured over HER when significant accumulation of oxides was observed[33]. While the pulse parameters in ref. [33] differ from those in our work, this study provides additional evidence that strongly oxidized copper surfaces can lead to efficient CO_2 conversion to CO.

The coexistence of metallic and oxidized Cu species is also the key factor for enhanced ethanol formation. As predicted by density functional theory modelling[11,34,35] and corroborated also by recent experimental infrared spectroscopy and in situ XAS data[36], the asymmetry between CO adsorption energies on metallic and oxidized copper sites facilitates CO dimerization and is essential for C_2 product formation[34]. Nevertheless, the more complex shape of the pulse duration dependency for ethanol production as compared with CO suggests that not only the amount but also the type of copper oxide formed during the anodic regime play a role in the increased ethanol yield. The enhancement in ethanol is observed only for the shortest anodic pulses ($\Delta t_a < 1$ s, region B), where the distorted oxide structure (as seen from our XRD and XAS data) is formed, featuring also some contribution of Cu(II) species (oxides or hydroxides, Fig. 4b). We consider these distorted oxide or hydroxide species, in close contact with metallic copper, to be the crucial sites for the ethanol production. Importantly, an increase of Δt_a results in an increased thickness of the oxide layer that adopts a structure that increasingly resembles the structure of bulk Cu_2O (region C). The latter results in the loss of the enhanced ethanol production. Similarly, the reduction of Δt_c below ~1 s leads to an incomplete reduction of the oxide layer during the cathodic pulse (Fig. 4c), resulting in the gradual accumulation of the oxide and the formation of a thicker Cu_2O shell with bulk-like structure (region D). As a consequence, the enhancement in the ethanol production is not pronounced for $\Delta t_c < 1$ s. The observed peak of the ethanol formation at $\Delta t_c \approx 4$ s and $\Delta t_a < 1$ s corresponds to the optimal ratio between distorted oxidic and metallic copper sites.

Our advanced operando X-ray studies thus revealed the complex interplay between a (reversible) oxide formation and the catalytic function of oxide-derived cubic copper nanocatalysts. We show the crucial role of the catalyst's surface repopulation with distorted multivalent copper oxide species that boost ethanol production. In contrast, extensive bulk-like copper-oxide formation prevents CO dimerization and rather facilitates CO formation. The observed dependency of the catalyst selectivity on the parameters of the applied pulsed CO_2RR protocol provides opportunities for steering the catalyst's selectivity on demand.

Methods

Catalyst synthesis. Cu_2O NCs were prepared by adapting a synthesis recipe described in a previous work[37]. Briefly, 4 ml 0.1 M $CuSO_4$ (Sigma-Aldrich, >98%) was diluted in 366 ml H_2O and stirred vigorously. Then 14 ml 1 M NaOH (Alfa Aesar, >97%) was added to start the nucleation process, while the reduction and NC growth were initialized by adding 16 ml of 0.25 M L-ascorbic acid (Sigma-Aldrich, reagent grade) after 10 s. The solution was stirred further for 13 min. The obtained sample was washed two times with an EtOH:H_2O mixture (1:1) and once with EtOH. The clean sample, with a copper concentration of 1.2 mg ml^{-1}, as determined by ICP-MS, was stored in 20 ml of EtOH. The electrodes were prepared by drop-casting 42 µl of the former solution on both sides of 1 cm^2 carbon paper (Alfa Aesar, Toray Carbon Paper, GGP-H-60). The total copper loading was 50 µg.

Electrocatalytic measurements. Electrocatalytic measurements were performed with an Autolab (Metrohm) potentiostat in a H-type cell equipped with an anion-exchange membrane (Selemion AMV, AGC) separating the cathodic and the anodic compartments. A leak-free Ag/AgCl reference electrode (LF-1, Alvatek) was set close to the working electrode in the cathodic compartment. A platinum gauze electrode (MaTecK, 3,600 mesh cm^{-2}) served as the counter-electrode in the anodic compartment. As electrolyte, 0.1 M $KHCO_3$ (Alfa Aesar, 99.7–100.5%) was purified with a cation-exchange resin (Chelex 100 Resin, Bio-Rad) and saturated with CO_2 (99.995%) for at least 20 min. Online products were determined for the static CO_2RR conditions by taking an aliquot of the electrolyte every 15 min.

After applying a linear sweep voltammogram from the open circuit potential to −1.0 V at 20 mV s^{-1}, a potential pulse protocol was carried out with fixed cathodic potential $E_c = -1.0$ V, anodic potential $E_a = +0.6$ V and different lengths of cathodic and anodic pulses. The linear sweep step was omitted for the data points with low Δt_c and Δt_a values, since in this case it contributed non-negligibly to the final yields of reaction products. The pulse sequence was repeated for 4,000 s. For comparison, after pulsing, another chronoamperometric measurement at constant −1.0 V was performed for 4,000 s.

Gas products were detected and quantified after 1 min and every 15 min by online gas chromatography (GC, Agilent 7890B), equipped with a thermal conductivity detector and a flame ionization detector. Liquid products were analysed after each measurement with a high-performance liquid chromatograph (Shimadzu Prominence), equipped with a NUCLEOGEL SUGAR 810 column and a refractive index detector, and a liquid GC (Shimadzu 2010 plus), equipped with a fused silica capillary column and a flame ionization detector. Each presented data point was measured at least three times, and we report the average values.

All catalytic results in this study are shown in terms of FE. The FE of the gas products was calculated as:

$$\mathrm{FE}_x = \frac{\dot{V} \times C_x \times z_x \times F}{A \times V_M \times j_{\mathrm{total}} \times \frac{\Delta t_c}{\Delta t_c + \Delta t_a}} \times 100\% \quad (1)$$

The FE for liquid products (which cannot be measured online, but only after a certain time under pulsed CO_2RR) was calculated as $\mathrm{FE}_x = \frac{V \times \Delta C_x \times z_x \times F}{\Delta Q} \times 100\%$. The factor $\frac{\Delta t_c}{\Delta t_c + \Delta t_a}$ is used in the FE expression for the gas products to weight j_{total} according to the total time spent by the catalyst in the Faradaic (cathodic) potential regime. In contrast, for liquid products ΔQ already contains the contribution of the pulse times by integrating the cathodic charge. Here FE_x is the FE of product x, $\dot{V}$ is the CO_2 gas flow rate (l s^{-1}), C_x is the volume fraction of the product x detected by GC, z_x is the number of electrons transferred for reduction to product x, F is the Faraday constant (C mol^{-1}), A is the geometric area of the electrode (cm^2), V_M is the molar volume (22.41 mol^{-1}), j_{total} is the total current density during CO_2 bulk electrolysis (A cm^{-2}), $\frac{\Delta t_c}{\Delta t_c + \Delta t_a}$ is a factor to account for the effective CO_2RR time of j_{total} while pulsing, ΔC_x is the accumulated concentration of product x detected by HPLC or liquid GC (mol l^{-1}), ΔQ is the total charge transfer during the electrolysis at constant potential or current (C) and V is the volume of the electrolyte (l).

The electrochemical surface area after 1 h reduction at −1.0 V was obtained by double-layer capacitance with cyclic voltammetry in the non-Faradaic region with variable scan rates. The resulting capacitance of 0.23(2) mF cm^{-2} corresponds to a 8.5-fold higher surface area compared to the copper foil (0.027 mF). Cyclic voltammetry was carried out between +0.3 and +0.45 V versus RHE, with scan rates of 20, 40, 60, 80, 100, 120 and 140 mV s^{-1}. The amount of dissolved copper in the electrolyte after CO_2RR was determined by ICP-MS (iCAP RQ, Thermo Fisher Scientific). See Supplementary Note 1 for more details on the analysis of electrocatalytic measurement data.

Characterization of catalyst morphology and composition. The morphology of the catalysts before and after CO_2RR was characterized by transmission electron microscopy (TEM). TEM measurements were performed using a Thermo Fisher 300 kV Titan microscope. The catalysts after CO_2RR were sonicated in 200 µl isopropanol to detach the sample and drop-cast on a nickel lacey carbon grid.

The surface composition of the copper catalysts was determined by quasi in situ XPS in the as-prepared state of the catalyst, after 1 h reduction under static CO_2RR and after 1 h under pulsed CO_2RR. Following the approach established in our previous work to determine the oxidation state at the cathodic and anodic pulse[10], the catalytic procedure was interrupted at the respective potential, the sample was washed with water at open circuit potential and directly transferred into an ultra-high-vacuum system for XPS measurements without exposure to air. The ultra-high-vacuum system system was equipped with an X-ray source (XR 50, SPECS) and a hemispherical electron analyser (Phoibos 100, SPECS, $E_{pass} = 15$ eV) and an aluminium anode (Al K_α, $h\nu = 1{,}486.6$ eV, 300 W).

Operando XAS measurements and data analysis. To collect X-ray absorption fine structure (XAFS) data, operando time-resolved XAS experiments at the Cu K-edge (8,979 eV) were carried out in quick XAFS (QXAFS) mode at the SuperXAS beamline at the SLS synchrotron (Switzerland). Additional experiments were carried out at the P64 beamline of the PETRA III synchrotron (Germany). In both cases the experiments were carried out in fluorescence mode using a home-made in situ cell for electrochemical measurements. A schematic of the cell is shown in ref. [38]. A platinum mesh and leak-free Ag/AgCl electrode were used as counter-electrode and reference electrode, respectively. The sample was deposited on carbon paper (Sigracet 29 BC, SGL Carbon), with the other side of the substrate covered with Kapton tape. The sample loading used in our operando XAS experiments was 500 μg cm^{-2}: this is the maximal loading of the sample that allows us to collect data of good quality, but is still sufficiently low to avoid self-absorption effects in fluorescence XAS data. The sample was mounted in the electrochemical cell with its Kapton-covered side acting as a window for incident and fluorescent radiation, while the side coated with the catalyst was in contact with the electrolyte. As electrolyte we used CO_2-saturated 0.1 M $KHCO_3$, which was continuously circulated through the cell using a peristaltic pump. CO_2 flow (20 ml min^{-1}) was ensured through the cell. The applied potential was controlled with a BioLogic (in the experiments at SuperXAS) or an Autolab (in experiments at DESY) potentiostat.

In the SuperXAS set-up, the super-bending magnet was used as X-ray source. A silicon-coated collimating mirror and platinum-coated toroidal refocusing mirror were used to remove higher-order harmonics, control the beam size and reduce heat load on the monochromator. A Si(111) channel-cut monochromator designed for high-speed scans was used for energy selection. The monochromator oscillated with a 5 Hz frequency, resulting in five XAFS spectra being collected every second. The beam size was 30 μm × 2.5 mm. At P64, a tapered undulator was used as the X-ray source, a Si(111) channel-cut monochromator was used for fast energy selection, and the beam size was less than 2 mm × 2 mm. The monochromator oscillation frequency was 1 Hz in this case. In both cases a PIPS detector was used for fluorescence intensity measurements. The intensity of the incident radiation was monitored by a gas chamber filled with nitrogen.

For measurements in QXAFS mode, calibration of the acquired data is essential. For this purpose, we mounted on the surface of our cell a thin CuO pellet, the fluorescence signal from which was used as a reference. Each scan began with the pellet being in the beam, then the sample stage was moved to bring our sample into the beam. To align the spectra, the energy scale for the collected QXAFS spectra was then shifted so that the maximum of the first derivative for the first QXAFS spectrum, which corresponds to the signal from the CuO pellet, is at the same energy as the maximum of the first derivative for the standard CuO spectrum, collected independently at the same beamline. Data calibration was performed using dedicated beamline-specific software (Pro-QEXAFS at SuperXAS, and JAQ at P64)[39]. Further data alignment, background subtraction, normalization, averaging and linear combination fitting of XANES spectra were performed using a set of Wolfram Mathematica scripts. EXAFS data extraction from averaged data was performed using Athena software[40].

EXAFS data fitting for the first coordination shell was performed using the FEFFIT code[40]. Theoretical phases and amplitudes were obtained in self-consistent ab initio calculations with FEFF8.5[41] for bulk copper, Cu_2O and CuO materials. The complex exchange-correlation Hedin–Lundqvist potential and default values of muffin-tin radii as provided within the FEFF8.5 code were employed.

We started with single-shell fitting of the copper foil and Cu_2O data to obtain the values of the amplitude reduction factors S_0^2. The obtained values were used later for the fitting of the experimental EXAFS data for nanocatalysts. Fitting of spectra for reference materials was carried out in the same ranges in k- and R-spaces as the ones later used for the nanocatalysts, to partially compensate for systematic errors due to the limited signal length in k-space. Fitting of EXAFS spectra $\chi(k)k^2$ thus was carried out in R-space in the range from $R_{min} = 1.1$ Å up to $R_{max} = 2.8$ Å. Fourier transform was carried out in the k range from 2.0 Å^{-1} up to 11.5 Å^{-1}. Fitting parameters were the coordination numbers N and interatomic distances R and disorder factors σ^2 for Cu–O and Cu–Cu bonds, and the corrections to photoelectron reference energies ΔE_0.

Operando high-energy XRD measurements and data analysis. Operando time-resolved high-energy XRD experiments were conducted at the Swedish Materials Science Beamline (P21.2) at Petra III. P21.2 is an undulator beamline equipped with a cryogenically cooled double Laue Si(111) monochromator. The X-ray energy was set to 67 keV ($\lambda = 0.18505$ Å) and a working distance of 0.895 m was calibrated using the diffraction pattern of a CeO_2 standard. The diffraction patterns were recorded using a Dectris Pilatus X CdTe 2 M, which is a large-area detector especially suitable for time-resolved high-energy XRD experiments. The acquisition time of the individual detector images was set to 10 s under stationary conditions and to 0.127 s for the time-resolved pulse experiments. Primary data treatment (calibration, masking, detector image integration) was conducted using the software package pyFAI[42].

A home-made electrochemical cell based on a three-electrode configuration using a leak-free miniature Ag/AgCl reference electrode (3.4 M KCl, eDAQ ET072) and a platinum counter-electrode[43]. A depiction of the operando XRD set-up can be found in Supplementary Fig. 2. The electrode potentials were controlled using a Biologic SP-240 potentiostat. The electrode potential and current were recorded together with XRD data to allow precise synchronization of the collected images and the electrode potential. The copper NCs were deposited on the microporous layer of the gas diffusion electrode (Sigracet 29 BC, SGL Carbon) with a loading of 0.3 mg_{Cu} cm^{-2}. For the operando high-energy XRD experiments, the sample was mounted and, subsequently, the operando X-ray cell was filled with the electrolyte. For alignment, the cell was centred and the gas diffusion electrode was aligned parallel to the X-ray beam using the beam stop diode. Subsequently, the incident X-ray angle was tuned between 0° and 1° to ensure an optimal Cu_2O to graphite Bragg peak ratio, and to ensure a sufficiently small spread of the X-rays on the sample, thus avoiding parasitic peak broadening.

After acquisition of the diffraction pattern under open-circuit conditions, a CO_2RR potential (−1 V versus RHE) was applied for at least 90 min to ensure the reduction of the catalyst. CO_2 was continuously bubbled through the electrolyte to ensure a stable pH. The electrolyte was frequently exchanged to avoid product accumulation.

The data analysis of the diffraction patterns after integration of the detector images was conducted using a set of GNU Octave scripts to perform background pattern subtraction, peak fitting using Lorentz profiles and averaging of the XRD data collected under pulsed CO_2RR. In the latter case, the averaging of the XRD data was conducted after correcting the peak profiles for lo- frequency variations due to, for example, bubble formation.

We limited the analysis to Cu(311), Cu_2O(111) and Cu_2O(220) Bragg peaks due to their sufficient intensity and minimal overlap with other Bragg peaks. The coherence length (size) of the crystalline domains was estimated from the individual Bragg peaks using the Scherrer equation based on the FWHM with a shape factor of 0.89. The lattice strain was calculated as $(d - d_0)/d_0$, where d_0 is the corresponding lattice spacing determined for the catalyst under the cathodic pulse from the Bragg peak position. The lattice parameter a of copper was calculated as $\sqrt{h^2 + k^2 + l^2}d$.

For comparison of pulsed CO_2RR conditions realized in different electrochemical cell set-ups, it is critical to ensure that the resistor-capacitor (RC) time constant is shorter than the duration of the studied pulses. In all our cells, we confirmed that this condition if fulfilled and does not limit the studied processes. The RC constants were determined by measuring the double-layer capacitance and the ohmic cell resistance in each cell used upon catalyst pre-reduction. In the H-type cell used for the selectivity measurements, an RC time constant of 38.7 ms (with $C = 2.87$ mF and $R = 13.5\,\Omega$) was determined for catalysts with the highest catalyst loading considered in our study (500 μg cm^{-2}). This value is much shorter than the shortest pulse length applied (0.5 s). Lower catalyst loadings led to similar time constants. In our operando XAS cell, the electrode area is twice as large, and the typical resistance is 20 Ω. For our XRD cell, the resistance is 40–50 Ω. The latter was used with a lower catalyst loading (300 μg/cm^2) with an electrode area of 6% of the one used for the XAS measurements.

Data availability

Catalytic activity data and processed XAS and XRD data are provided in the Supplementary Information. The raw XAS and XRD data (which require specialized software to process), and all other data that support the findings of this study are available from the corresponding authors on reasonable request.

Received: 5 July 2021; Accepted: 28 February 2022;
Published online: 21 April 2022

References

1. Hori, Y., Kikuchi, K. & Suzuki, S. Production of CO and CH_4 in electrochemical reduction of CO_2 at metal electrodes in aqueous hydrogencarbonate solution. *Chem. Lett.* **14**, 1695–1698 (1985).
2. Mistry, H., Varela, A. S., Kuehl, S., Strasser, P. & Roldan Cuenya, B. Nanostructured electrocatalysts with tunable activity and selectivity. *Nat. Rev. Mater.* **1**, 16009 (2016).
3. Gao, D., Arán-Ais, R. M., Jeon, H. S. & Roldan Cuenya, B. Rational catalyst and electrolyte design for CO_2 electroreduction towards multicarbon products. *Nat. Catal.* **2**, 198–210 (2019).
4. Xie, H., Wang, T., Liang, J., Li, Q. & Sun, S. Cu-based nanocatalysts for electrochemical reduction of CO_2. *Nano Today* **21**, 41–54 (2018).

5. Fan, L. et al. Strategies in catalysts and electrolyzer design for electrochemical CO_2 reduction toward C_{2+} products. *Sci. Adv.* **6**, eaay3111 (2020).
6. Mistry, H. et al. Highly selective plasma-activated copper catalysts for carbon dioxide reduction to ethylene. *Nat. Commun.* **7**, 12123 (2016).
7. Zhou, Y. et al. Dopant-induced electron localization drives CO_2 reduction to C_2 hydrocarbons. *Nat. Chem.* **10**, 974–980 (2018).
8. Shiratsuchi, R., Aikoh, Y. & Nogami, G. Pulsed electroreduction of CO_2 on copper electrodes. *J. Electrochem. Soc.* **140**, 3479–3482 (1993).
9. Engelbrecht, A. et al. On the electrochemical CO_2 reduction at copper sheet electrodes with enhanced long-term stability by pulsed electrolysis. *J. Electrochem. Soc.* **165**, J3059–J3068 (2018).
10. Arán-Ais, R. M., Scholten, F., Kunze, S., Rizo, R. & Roldan Cuenya, B. The role of in situ generated morphological motifs and Cu(I) species in C_{2+} product selectivity during CO_2 pulsed electroreduction. *Nat. Energy* **5**, 317–325 (2020).
11. Lin, S.-C. et al. Operando time-resolved X-ray absorption spectroscopy reveals the chemical nature enabling highly selective CO_2 reduction. *Nat. Commun.* **11**, 3525 (2020).
12. Jannsch, Y. Pulsed potential electrochemical CO_2 reduction for enhanced stability and catalyst reactivation of copper electrodes. *Electrochem. Commun.* **121**, 106861 (2020).
13. Kimura, K. W. et al. Controlled selectivity of CO_2 reduction on copper by pulsing the electrochemical potential. *ChemSusChem* **11**, 1781–1786 (2018).
14. Lee, J. & Tak, Y. Electrocatalytic activity of Cu electrode in electroreduction of CO_2. *Electrochim. Acta* **46**, 3015–3022 (2001).
15. Ishimaru, S., Shiratsuchi, R. & Nogami, G. Pulsed electroreduction of CO_2 on Cu–Ag alloy electrodes. *J. Electrochem. Soc.* **147**, 1864–1867 (2000).
16. Kimura, K. W. et al. Selective electrochemical CO_2 reduction during pulsed potential stems from dynamic interface. *ACS Catal.* **10**, 8632–8639 (2020).
17. Kim, C., Weng, L.-C. & Bell, A. T. Impact of pulsed electrochemical reduction of CO2 on the formation of C_{2+} products over Cu. *ACS Catal.* **10**, 12403–12413 (2020).
18. Tang, Z., Nishiwaki, E., Fritz, K. E., Hanrath, T. & Suntivich, J. Cu(I) reducibility controls ethylene vs ethanol selectivity on (100)-textured copper during pulsed CO_2 reduction. *ACS Appl. Mater. Inter.* **13**, 14050–14055 (2021).
19. Jeon, H. S. et al. Selectivity control of Cu nanocrystals in a gas-fed flow cell through CO_2 pulsed electroreduction. *J. Am. Chem. Soc.* **143**, 7578–7587 (2021).
20. Lei, Q. et al. Investigating the origin of enhanced C_{2+} selectivity in oxide-/hydroxide-derived copper electrodes during CO_2 electroreduction. *J. Am. Chem. Soc.* **142**, 4213–4222 (2020).
21. Gupta, N., Gattrell, M. & MacDougall, B. Calculation for the cathode surface concentrations in the electrochemical reduction of CO_2 in $KHCO_3$ solutions. *J. Appl. Electrochem.* **36**, 161–172 (2006).
22. Casebolt, R. et al. Effect of electrolyte composition and concentration on pulsed potential electrochemical CO_2 reduction. *ChemElectroChem* **8**, 681–688 (2021).
23. Herzog, A. et al. Operando investigation of Ag-decorated Cu_2O nanocube catalysts with enhanced CO_2 electroreduction toward liquid products. *Angew. Chem. Int. Ed.* **60**, 7426–7435 (2021).
24. Möller, T. et al. Electrocatalytic CO_2 reduction on CuO_x nanocubes: tracking the evolution of chemical state, geometric structure, and catalytic selectivity using operando spectroscopy. *Angew. Chem. Int. Ed.* **132**, 18130–18139 (2020).
25. Gao, D. et al. Plasma-activated copper nanocube catalysts for efficient carbon dioxide electroreduction to hydrocarbons and alcohols. *ACS Nano* **11**, 4825–4831 (2017).
26. Grosse, P. et al. Dynamic changes in the structure, chemical state and catalytic selectivity of Cu nanocubes during CO_2 electroreduction: size and support effects. *Angew. Chem. Int. Ed.* **57**, 6192–6197 (2018).
27. Arán-Ais, R. M. et al. Imaging electrochemically synthesized Cu_2O cubes and their morphological evolution under conditions relevant to CO_2 electroreduction. *Nat. Commun.* **11**, 3489 (2020).
28. Grosse, P., Yoon, A., Rettenmaier, C., Chee, S. W. & Cuenya, B. R. Growth dynamics and processes governing the stability of electrodeposited size-controlled cubic Cu catalysts. *J. Phys. Chem. C.* **124**, 26908–26915 (2020).
29. Grosse, P. et al. Dynamic transformation of cubic copper catalysts during CO_2 electroreduction and its impact on catalytic selectivity. *Nat. Commun.* **12**, 6736 (2021).
30. Navarro, J. J. et al. Structure of a silica thin film on oxidized Cu(111): conservation of the honeycomb lattice and role of the interlayer. *J. Phys. Chem. C.* **124**, 20942–20949 (2020).
31. Simon, G. H., Kley, C. S. & Roldan Cuenya, B. Potential-dependent morphology of copper catalysts during CO_2 electroreduction revealed by in situ atomic force microscopy. *Angew. Chem. Int. Ed.* **60**, 2561–2568 (2021).
32. LaGrow, A. P., Ward, M. R., Lloyd, D. C., Gai, P. L. & Boyes, E. D. Visualizing the Cu/Cu_2O interface transition in nanoparticles with environmental scanning transmission electron microscopy. *J. Am. Chem. Soc.* **139**, 179–185 (2017).
33. Kumar, B. et al. Controlling the product syngas H_2: CO ratio through pulsed-bias electrochemical reduction of CO_2 on copper. *ACS Catal.* **6**, 4739–4745 (2016).
34. Xiao, H., Goddard, W. A., Cheng, T. & Liu, Y. Cu metal embedded in oxidized matrix catalyst to promote CO_2 activation and CO dimerization for electrochemical reduction of CO_2. *Proc. Natl Acad. Sci. USA* **114**, 6685–6688 (2017).
35. Dattila, F., Garcia-Muelas, R. & López, N. R. Active and selective ensembles in oxide-derived copper catalysts for CO_2 reduction. *ACS Energy Lett.* **5**, 3176–3184 (2020).
36. Chou, T.-C. et al. Controlling the oxidation state of the Cu electrode and reaction intermediates for electrochemical CO_2 reduction to ethylene. *J. Am. Chem. Soc.* **142**, 2857–2867 (2020).
37. Ke, W. H., Hsia, C. F., Chen, Y. J. & Huang, M. H. Synthesis of ultrasmall Cu_2O nanocubes and octahedra with tunable sizes for facet-dependent optical property examination. *Small* **12**, 3530–3534 (2016).
38. Timoshenko, J. & Roldan Cuenya, B. In situ/operando electrocatalyst characterization by X-ray absorption spectroscopy. *Chem. Rev.* **121**, 882–961 (2021).
39. Bornmann, B., Kläs, J., Müller, O., Lützenkirchen-Hecht, D. & Frahm, R. The quick EXAFS setup at beamline P64 at PETRA III for up to 200 spectra per second. *AIP Conf. Proc.* **2054**, 040008 (2019).
40. Ravel, B. & Newville, M. ATHENA, ARTEMIS, HEPHAESTUS: data analysis for X-ray absorption spectroscopy using IFEFFIT. *J. Synchrotron Radiat.* **12**, 537–541 (2005).
41. Ankudinov, A. L., Ravel, B., Rehr, J. J. & Conradson, S. D. Real-space multiple-scattering calculation and interpretation of X-ray-absorption near-edge structure. *Phys. Rev. B* **58**, 7565–7576 (1998).
42. Ashiotis, G. et al. The fast azimuthal integration Python library: pyFAI. *J. Appl. Crystallogr.* **48**, 510–519 (2015).
43. Reikowski, F. et al. Operando surface X-ray diffraction studies of structurally defined Co_3O_4 and CoOOH thin films during oxygen evolution. *ACS Catal.* **9**, 3811–3821 (2019).

Acknowledgements

Financial support was provided by the European Research Council (ERC-725915, OPERANDOCAT), the German Research Foundation (DFG, project numbers 406944504 and SPP 2080) and Germany´s Excellence Strategy (EXC 2008, 390540038, UniSysCat). We acknowledge the Paul Scherrer Institute, Villigen, Switzerland, and DESY (Germany), a member of the Helmholtz Association HGF, for synchrotron radiation beamtime. We thank A. Clark and M. Nachtegaal for assistance in using the SuperXAS beamline of the SLS, V. Murzin and W. Caliebe for assistance in using the P64 beamline of PETRA III, and Z. Hegedues and U. Lienert for assistance in using the P21.2 beamline of PETRA III.

Author contributions

J. Timoshenko, A.B., C.R. and B.R.C. co-wrote the paper. B.R.C. designed and supervised the study. J. Timoshenko designed and supervised the operando XAS experiments. A.B. designed and supervised the operando XRD experiments. C.R. performed sample synthesis (with contribution from A.H.), characterization (with contribution from P.G. and S.K.) and designed and performed catalytic activity studies. J. Timoshenko, A.B., C.R., R.M.A-A., H.S.J., F.T.H., A.H., U.H., E.M.D., J. Tian and O.M. participated in planning and realization of the synchrotron experiments. All authors contributed to the discussion and interpretation of the results and editing the manuscript.

Funding

Open access funding provided by Max Planck Society.

Competing interests

The authors declare no competing interests.

Additional information

Supplementary information The online version contains supplementary material available at https://doi.org/10.1038/s41929-022-00760-z.

Correspondence and requests for materials should be addressed to Janis Timoshenko or Beatriz Roldan Cuenya.

Peer review information *Nature Catalysis* thanks Jinghua Guo and the other, anonymous, reviewer(s) for their contribution to the peer review of this work.